Supplement of Biogeosciences, 23, 3159–3178, 2026
https://doi.org/10.5194/bg-23-3159-2026-supplement

Biogeosciences Open Access EGU

Supplement of

Linking surface coverage with surfactant activity to refine the role of surfactants for air-sea gas exchange

Falko Asmussen-Schäfer et al.

Correspondence to: Gernot Friedrichs (friedrichs@phc.uni-kiel.de)

Contents

S1. Polarization-resolved SFG spectra of natural samples

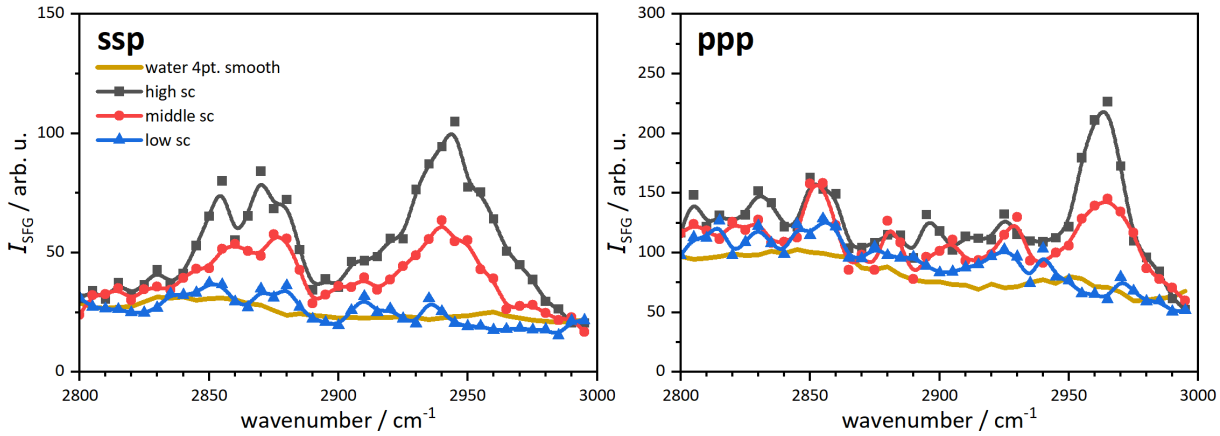

Figure S1: Comparison of VSFG measurements in ssp and ppp polarization combinations for selected Helgoland SML samples exhibiting high, medium, and low surfactant surface coverage. Each SML spectrum corresponds to a single measurement. Solid lines represent B-spline fits to guide the eye.

To further evaluate potential structural or orientational effects, selected Helgoland samples exhibiting high, medium, and low surfactant surface coverage were re-measured in both ssp and ppp polarization combination. Note that these measurements were performed on samples that had been stored frozen in the laboratory for months after the main data analysis took place.

A direct comparison of the ssp and ppp spectra is presented in Fig. S1. Both polarization combinations exhibit the characteristic spectral features of alkyl-containing surfactants. A detailed peak assignment for the ssp spectra is provided in the main text. The ppp spectrum is largely dominated by a single intense band, which can be attributed to the antisymmetric CH_3 stretching vibration at around 2960 cm^{-1}. Across the low, medium, and high surface coverage samples, the intensity evolution in the ppp spectra mirrors the same trend as observed for the ssp polarization. The lack of additional bands and the consistent intensity trends indicate that the ppp-VSFG spectra do not point to notable changes in composition or to distinct structural or orientational differences of the probed alkyl groups in the natural SML samples investigated. Considering the generally higher signal-to-noise ratio and the comparatively high experimental effort, we therefore restricted our analysis to ssp measurements and, accordingly, defined the sc metric exclusively on the basis of the ssp spectra.

S2. Comparison of VSFG spectral trends

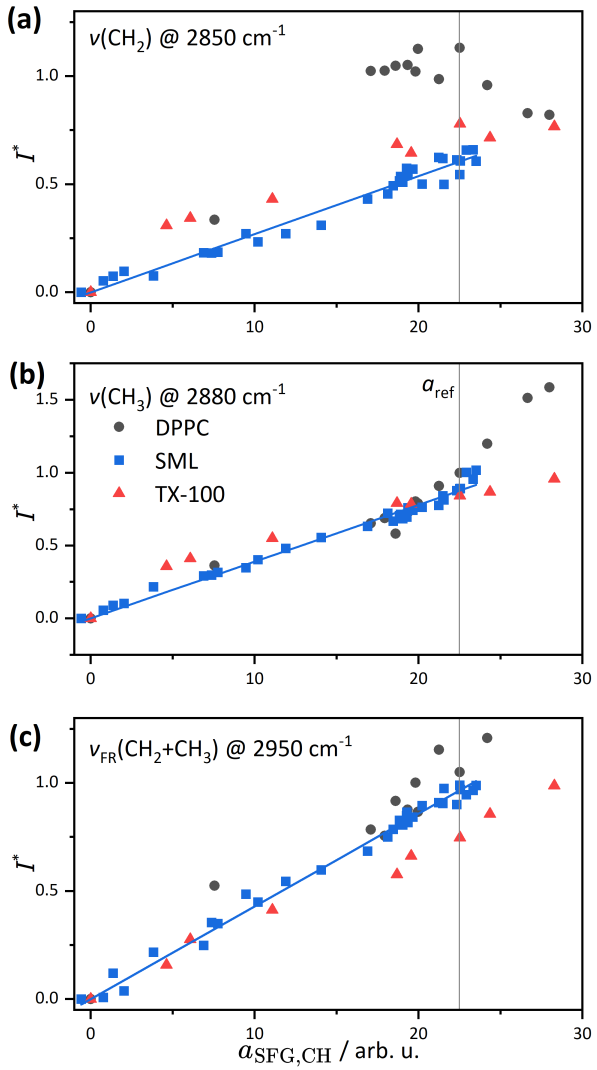

Figure S2: VSFG spectral trends. a) CH_2, b) CH_3, and c) Fermi resonance peaks in the VSFG spectra of SML, DPPC, and TX-100 samples.

In order to compare the spectral trends for different samples (SML, DPPC, TX-100), relative signal intensities I^* were calculated as follows:

$$I^* = \frac{\sqrt{\mathrm{I}_i} - \sqrt{\mathrm{I}_{\mathrm{H_2O}}}}{\sqrt{\mathrm{I}_{\mathrm{CH_3}}(a_{\text{SFG-CH, ref.}})} - \sqrt{\mathrm{I}_{\mathrm{H_2O}}}}$$

Here, the (water background-corrected) peak intensity values were arbitrarily normalized to the CH_3 peak intensity corresponding the VSFG spectrum of the DPPC reference point (see main paper Fig. 5, $\Pi = 4\,\mathrm{mN\,m^{-1}}$). Figure S2 shows the intensity trends for the three main vibrational bands of the symmetric C-H stretch vibrations of CH_2 (panel a) and CH_3 (panel b) as well as their corresponding Fermi resonance band (panel c) as function of the overall integrated C-H stretch

spectral intensity $a_{\text{SFG-CH}}$. In these plots, a linear dependence indicates that the corresponding relative peak contribution to the overall spectrum remains constant. For the SML samples, a linear correlation is obtained for all three vibrations, hence indicating that the overall spectral shape remains unchanged. This linear trend supports our assumption that a linear scaling of the surface coverage index sc as a function of the (rooted) VSFG spectral intensity according to Eqs. 2 and 3 is reasonable.

In contrast, distinct spectral changes are seen for DPPC. For example, toward higher spectral intensity, the I^* values of the $\nu(CH_2)$ peak remain nearly constant or even slightly decrease at the highest plotted $a_{\text{SFG-CH}}$ values. Instead, the intensity of the $\nu(CH_3)$ band rises disproportionately, resulting in a much stronger contribution of the $\nu(CH_3)$ band to the overall integrated spectral intensity. As discussed in the main text, this is due to the structural alignment of the alkyl chains at high DPPC surface concentrations, causing a pronounced surface concentration dependence of the underlying hyperpolarizibility $\beta(N)$ in Eq. 1.

TX-100 exhibits an intermediate characteristics. Compared to DPPC, the non-linearities are much less pronounced, but a leveling-off of the signal contributions from the $\nu(CH_2)$ and $\nu(CH_2$ bands is clearly visible. As discussed in the main text and as seen in Fig. 4, this is due to the prominent band at 2915 cm^{-1}, which we have assigned to the antisymmetric stretch vibration of the methylene group.

S3. Surface coverage data

Table S1: SURF mesocosm study 2023: Mean surface coverage and SML surfactant activity. Data are also available in PANGAEA (Bibi et al., 2025), and have been discussed previously in the context of biological drivers for surfactant formation in Bibi et al. (2025).

Date	surface coverage / %		SAS / µg Teq L^{-1}		Date	surface coverage / %		SAS / µg Teq L^{-1}	
May 17	3.4	± 4.5	1376	± 145	Jun 01	84.6	± 10.5	522	± 45
May 18	6.1	± 4.9	499	± 45	Jun 02	99.2	± 11.3	1445	± 52
May 19	-2.6	± 5.7	191	± 10	Jun 03	89.9	± 10.7	445	± 44
May 20	42.1	± 7.2	90	± 6	Jun 04	84.0	± 9.7	1963	± 71
May 21	17.0	± 4.9	138	± 7	Jun 05	86.0	± 10.0	1868	± 56
May 22	52.8	± 7.6	295	± 13	Jun 06	85.7	± 10.4	1410	± 75
May 23	30.6	± 6.9	138	± 22	Jun 07	95.5	± 10.9	717	± 3
May 24	34.5	± 6.4	294	± 35	Jun 08	87.3	± 10.0	1010	± 25
May 25	32.8	± 14.7	233	± 33	Jun 09	85.6	± 10.4	290	± 18
May 26	9.0	± 7.1	200	± 16	Jun 10	83.7	± 10.0	372	± 26
May 27	45.3	± 11.6	343	± 19	Jun 11	103.7	± 11.6	134	± 7
May 28	62.5	± 8.6	334	± 38	Jun 12	104.5	± 11.7	1179	± 31
May 29	82.0	± 9.6	401	± 41	Jun 13	101.9	± 12.1	341	± 40
May 30	75.1	± 10.8	327	± 28	Jun 14	100.2	± 11.3	1229	± 119
May 31	80.5	± 12.0	274	± 22	Jun 15	100.1	± 11.6	471	± 42

Table S2: Helgoland field campaign 2024: Mean surface coverage and surfactant activity data.

Date	surface coverage / %		SAS / µg Teq L^{-1}		category
Jul 21	78.8	± 58.2	79.5	± 32.8	SML slick
Jul 27	129.9	± 19.7	903.9	± 24.4	SML slick
Jul 27	101.7	± 64.5	301.3	± 30.1	SML slick
Jul 29	34.1	± 15.7	130.2	± 8.7	SML slick
Jul 29	61.5	± 12.8	86.2	± 24.6	SML slick
Jul 18	46.7	± 40.1	288.5	± 24.6	SML non-slick
Jul 27	25.3	± 16.3	240.1	± 18.8	SML non-slick
Jul 27	76.7	± 24.9	301.3	± 30.1	SML non-slick
Jul 29	43.8	± 17.4	130.2	± 8.7	SML non-slick
Jul 29	65.1	± 24.0	86.2	± 24.6	SML non-slick
Jul 15	-16.1	± 15.1	196.6	± 15.9	ULW
Jul 20	11.4	± 6.3	84.0	± 6.4	ULW
Jul 21	30.6	± 40.6	58.9	± 7.6	ULW
Jul 27	52.9	± 14.4	130.2	± 13.7	ULW
Jul 29	23.6	± 13.8	340.6	± 38.8	ULW

S4. Global surface coverage estimate

This section provides a more detailed explanation of the conceptional model for global surface coverage estimation as introduced in Section 3.4. The model links depth-integrated primary production to surfactant activity and surface coverage.

Primary production data were taken from Copernicus Marine Service (2024a), using the most recent data set for the year 2024 as an example. Primary production is provided as depth-integrated values by accounting for vertical layer thickness Δz_i, $PP_{\mathrm{int}} = \sum_i PP_i \cdot \Delta z_i$. This yields monthly or seasonally averaged depth-integrated primary production PP_{int} in units of $\mathrm{g\,C\,m^{-2}\,d^{-1}}$ (see Fig. S3).

Next, the integrated fields can be classified into three trophic zones (oligotrophic, mesotrophic, eutrophic). This allows us to use the resulting fields as an input for linking primary production to surfactant activity by adopting an empirical relationship. Wurl et al. (2011) estimated the global presence of surfactants based on comprehensive surfactant activity measurements and provided the necessary data to correlate surface activity with primary production. Figure S4 illustrates the resulting, seasonally averaged global maps using threshold values of $0.4\,\mathrm{g\,m^{-2}\,d^{-1}}$ and $1.2\,\mathrm{g\,m^{-2}\,d^{-1}}$ for oligotrophic, mesotrophic, and eutrophic regimes, respectively. In principle, each trophic zone could be assigned a single mean surfactant activity (320, 502, and 663 $\mu\mathrm{g\,Teq\,L^{-1}}$, from Wurl et al. (2011)) and a single mean surface coverage as well (65, 78 and 86 %, from our Langmuir-type correlation between surfactant activity and surface coverage). Already this simple approach reveals that expected surface coverage potential on the oceans is high, even for oligotrophic waters. However, such a simplistic approach levels out differences too much.

To better preserve the spatial resolution of the primary production dataset in the simulation, we proceeded as follows: First, the primary production data were analyzed with respect to their mean values within the three tropic trophic zones for each month (see Table S3). As it turned out that the monthly variability was rather small, the monthly data were subsequently averaged to obtain an annual mean. Secondly, these three values were assigned to the three mean surfactant activity values from Wurl et al. (2011)) and then fitted with a modified logistic saturation function with intercept (see Fig. S5) to derive a continuous correlation function between primary production and surfactant activity. The logistic-type function was chosen because (*i*) it reasonably represents the three data points, (*ii*) it can be confined to yield the lowest observed surfactant activity value of $104\,\mu\mathrm{g\,Teq\,L^{-1}}$ at zero primary production, and (*iii*) it monotonically increases up to a saturation threshold, where we have used the upper 2σ uncertainty limit of the eutrophic data reported by Wurl et al. (2011). Thirdly, this correlation function was used in combination with our Langmuir-type surfactant activity-surface coverage correlation (see Section 3.3) to predict global surfactant coverage values. Results of this procedure are shown as seasonally averaged surfactant activity maps in Fig. S6 and surface coverage potential maps in Fig. S7. The shaded areas mark regions where the mean wind speed is above $10\,\mathrm{m\,s^{-1}}$ (Copernicus Marine Service, 2024a,b) and the neglect of wind may lead to higher uncertainties.

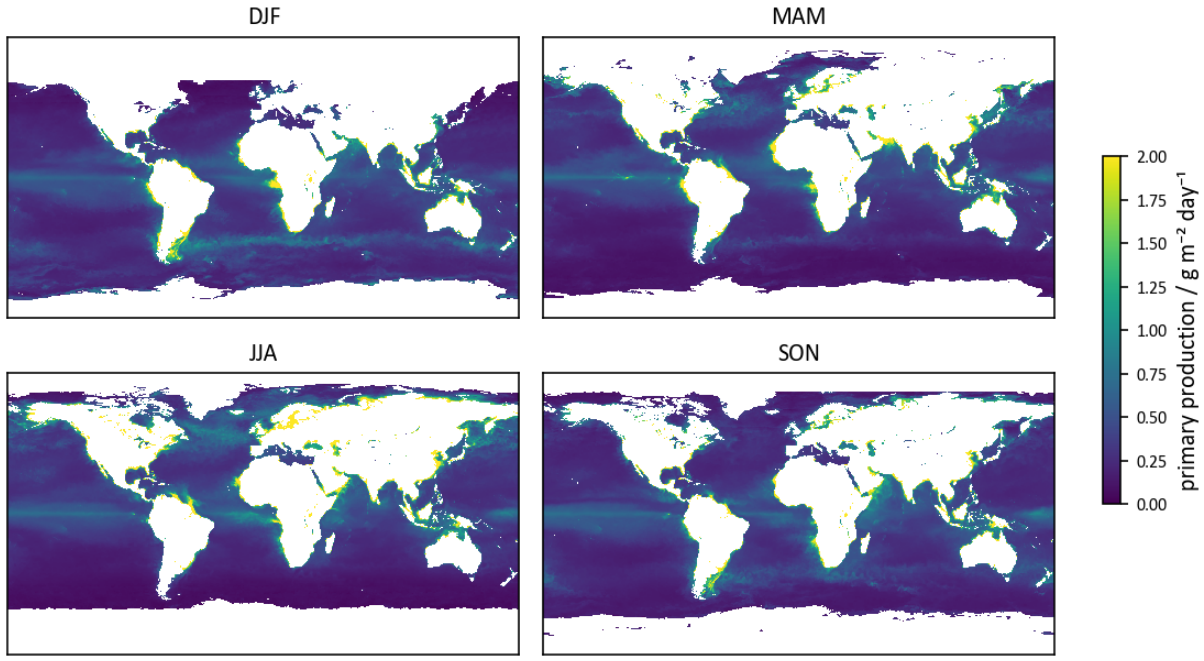

Figure S3: Global maps of primary production by seasons for 2024, based on satellite-derived data adopted from Copernicus Marine Service (2024a).

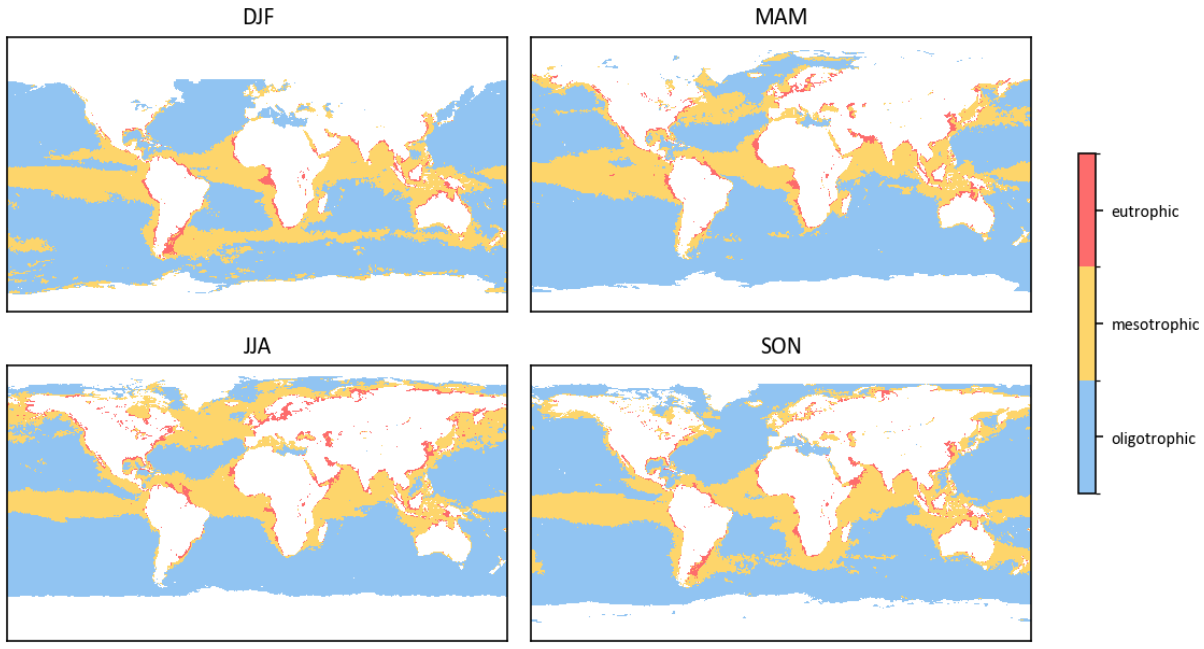

Figure S4: Trophic classification by seasons for 2024, based on primary productivity.

Table S3: Mean primary production per trophic zone for 2024.

Month	mean primary production / $\mathrm{g\,m^{-2}\,d^{-1}}$		
	eutroph	mesotroph	oligotroph
1	2.15	0.56	0.26
2	2.15	0.57	0.25
3	2.21	0.56	0.24
4	2.13	0.57	0.22
5	2.11	0.59	0.23
6	2.30	0.60	0.24
7	2.32	0.61	0.24
8	2.28	0.61	0.23
9	2.15	0.59	0.24
10	2.10	0.58	0.25
11	2.18	0.56	0.25
12	2.14	0.57	0.26
mean	2.18	0.58	0.24

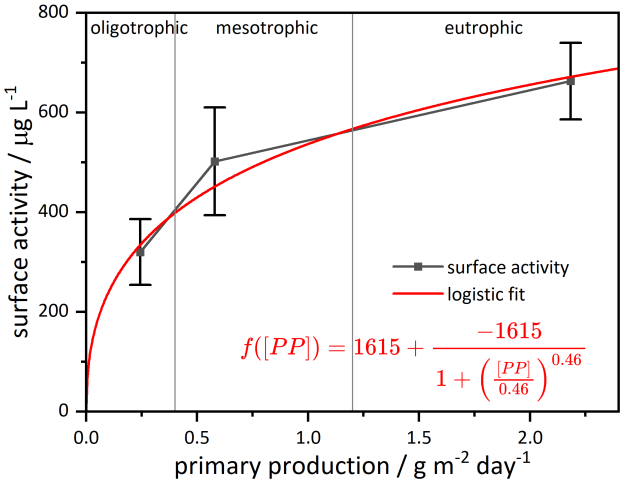

Figure S5: Surface activity - primary production correlation. The error bars represent the 95 % confidence intervall in Wurl et al. (2011). The logistic fit has been constrained to the lowest reported value at zero primary productivity and the saturation threshold was set equal to the upper 2σ uncertainty bound of the eutrophic data point.

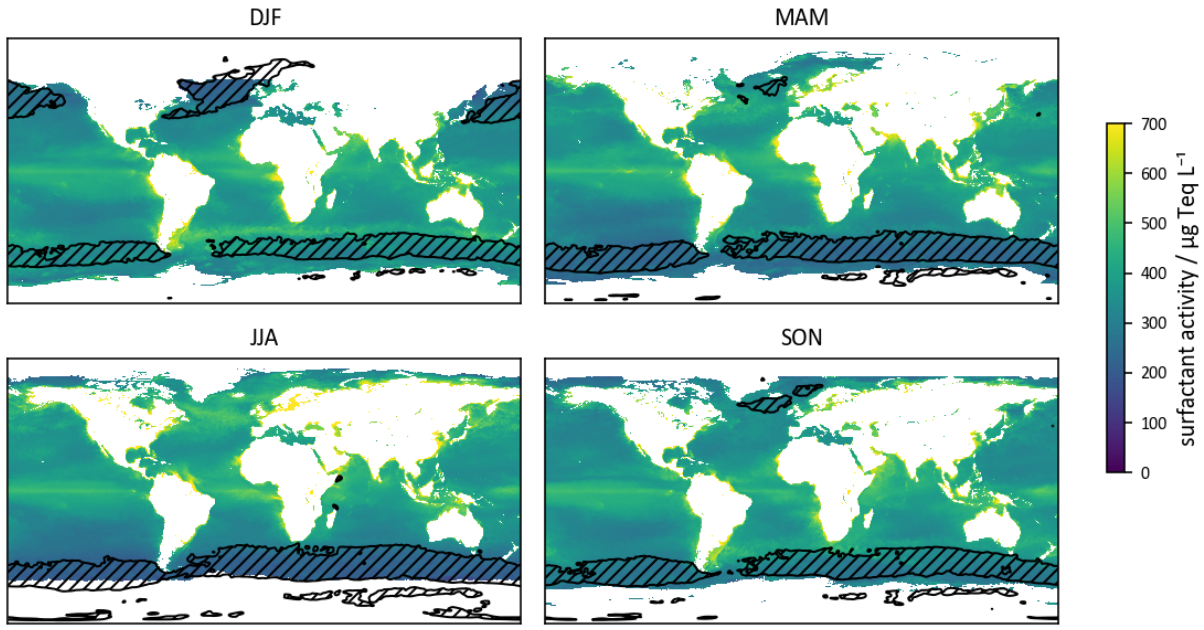

Figure S6: Global maps of surface activity by seasons for 2024, based on a assumed correlation with primary production. The hashed black area shows regimes where the mean wind speed is above $10\,\mathrm{m\,s^{-1}}$.

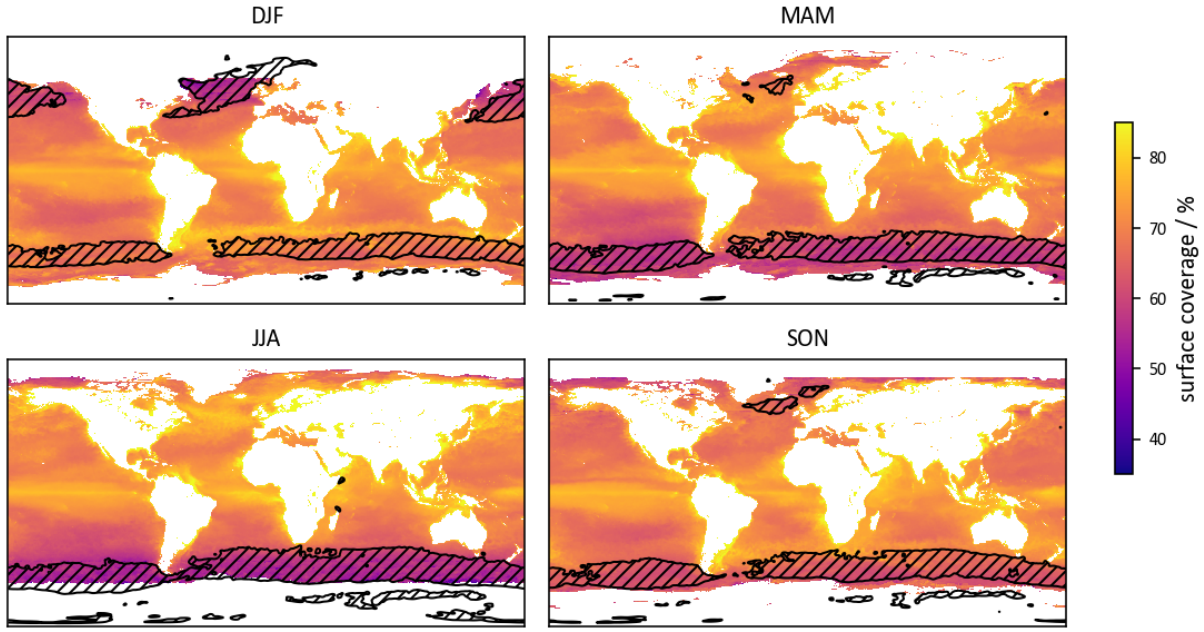

Figure S7: Global maps of surface coverage by seasons for 2024., based on a assumed Langmuir type correlation with surfactant activity data. The hashed black area shows regimes where the mean wind speed is above $10\,\mathrm{m\,s^{-1}}$.

S5. Role of surfactant surface coverage for wave damping

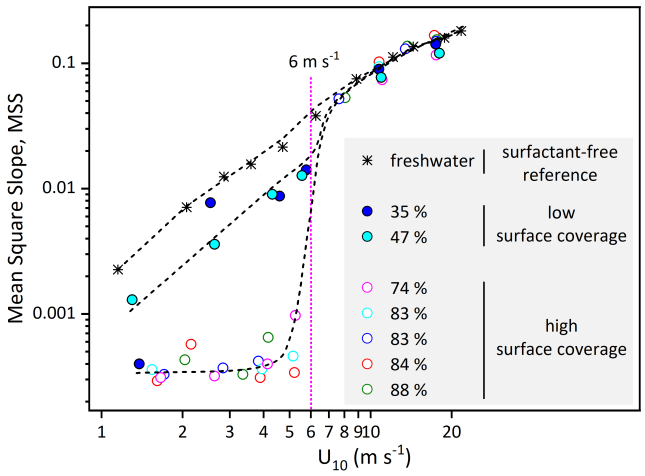

Figure S8: Reduction of mean square slope as a function of wind speed, u_{10}, for a surfactant-free freshwater reference experiment (stars) in comparison with experiments using natural seawater with high (open circles) or low (filled circles) surfactant surface coverage. The dashed curves serve as trend lines intended solely to aid visual interpretation. Surfactant data are adopted from Engel et al. (2026) and freshwater data from Krall (2013) and Kunz (2017).

Figure S8 presents wave damping measurements from experiments performed in the Heidelberg "Aeolotron" a large annular wind–wave tank containing 18.000 L of water. Freshwater reference data (stars) are taken from the dissertations of Krall (2013) and Kunz (2017) and are compared with results from an experiment using natural seawater enriched with organic matter published in a paper by Engel et al. (2026) (circles). Further details of the experimental setup are given in Engel et al. (2026). Figure S8 depicts how the observed wave field varies with wind speed, expressed via the mean square slope (MSS), a dimensionless measure of water surface roughness. MSS is directly linked to the gas transfer velocity; thus, higher MSS values indicate more efficient, predominantly turbulence-driven air–sea gas exchange. While the damping effect of a surfactant film vanishes at wind speeds above 6 m/s because the organic material is effectively mixed into the bulk water, pronounced wave damping is evident at lower wind speeds. The most substantial damping occurs in experiments with surfactant surface coverages approaching a fully developed film, $sc \geq 74\%$ (open circles), where the water surface is nearly completely flattened. By contrast, the two experiments with low surfactant coverages of 35% and 47% (filled circle) exhibit a much smaller reduction in MSS, yet still demonstrate a clear surfactant effect. Note that the sc values in Engel et al. (2026) were obtained using the same VSFG method employed in the present study, hence highlighting the strong coupling between the surface coverage metric with wave damping and air–sea gas exchange, potentially driven by surfactant-induced modulation of the surface tension.

References

Bibi, R., Ribas-Ribas, M., Jaeger, L., Lehners, C., Gassen, L., Cortés, E., Wollschläger, J., Thölen, C., Waska, H., Zöbelein, J., Brinkhoff, T., Athale, I., Röttgers, R., Novak, M., Engel, A., Barthelmeß, T., Karnatz, J., Reinthaler, T., Spriahailo, D., Friedrichs, G., Schäfer, F., and Wurl, O.: Physical, chemical, and biogeochemical parameters from a mesocosm experiment at the Sea Surface Facility (SURF), Wilhelmshaven, Germany, spring 2023, https://doi.org/10.1594/PANGAEA.984101, 2025.

Bibi, R., Ribas-Ribas, M., Jaeger, L., Lehners, C., Gassen, L., Cortés-Espinoza, E. F., Wollschläger, J., Thölen, C., Waska, H., Zöbelein, J., Brinkhoff, T., Athale, I., Röttgers, R., Novak, M., Engel, A., Barthelmeß, T., Karnatz, J., Reinthaler, T., Spriahailo, D., Friedrichs, G., Schäfer, F. A., and Wurl, O.: Biogeochemical dynamics of the sea-surface microlayer in a multidisciplinary mesocosm study, Biogeosciences, 22, 7563–7589, https://doi.org/10.5194/bg-22-7563-2025, 2025.

Copernicus Marine Service: Global Ocean Colour (Copernicus-GlobColour), Bio-Geo-Chemical, L4 (monthly and interpolated) from Satellite Observations (1997-ongoing), Tech. rep., https://doi.org/10.48670/moi-00281, accessed: 2025-10-09, 2024a.

Copernicus Marine Service: Global Ocean Monthly Mean Sea Surface Wind and Stress from Scatterometer and Model, Tech. rep., https://doi.org/10.48670/moi-00181, accessed: 2025-09-26, 2024b.

Engel, A., Friedrichs, G., Krall, K. E., and Jähne, B.: Wind-induced collapse of the biopolymeric surface microlayer induces sudden changes in sea surface roughness, Biogeosciences, 23, 2101–2117, https://doi.org/10.5194/bg-23-2101-2026, 2026.

Krall, K. E.: Laboratory Investigations of Air-Sea Gas Transfer under a Wide Range of Water Surface Conditions, Dissertation, Universität Heidelberg, Heidelberg, Germany, https://doi.org/10.11588/heidok.00014392, 2013.

Kunz, J.: Active Thermography as a Tool for the Estimation of Air-Water Transfer Velocities, Dissertation, Universität Heidelberg, Heidelberg, Germany, https://doi.org/0.11588/heidok.00022903, 2017.

Wurl, O., Wurl, E., Miller, L., Johnson, K., and Vagle, S.: Formation and global distribution of sea-surface microlayers, Biogeosciences, 8, 121–135, https://doi.org/10.5194/bg-8-121-2011, 2011.